

## Measurement of the ratio of the cesium $D$ -line transition strengths

Robert J. Rafac\* and Carol E. Tanner

University of Notre Dame, Notre Dame, Indiana 46556

(Received 29 December 1997)

High-precision laser absorption spectroscopy in a thermal vapor cell is used in the measurement of the ratio of the  $D$ -line transition strengths in the cesium atom. We find  $|\langle 6p^2P_{3/2} || \vec{r} || 6s^2S_{1/2} \rangle|^2 / |\langle 6p^2P_{1/2} || \vec{r} || 6s^2S_{1/2} \rangle|^2 = 1.9809(9)$ , which compares favorably with the ratio calculated from the most precise lifetime measurements of these states and the predictions of *ab initio* calculation. We also verify the predictions of impact-regime line-broadening calculations for densities of order  $10^{18}$  atoms per  $m^3$ . Theoretical implications and future experimental promise are discussed. [S1050-2947(98)05008-2]

PACS number(s): 32.70.Cs, 32.70.Jz, 32.70.-n, 34.90.+q

### I. INTRODUCTION

We have constructed a vapor cell absorption spectrometer for high-precision transition strength measurements in neutral cesium. Precise knowledge of the transition amplitudes between low-lying states in the cesium atom is of great importance to the testing of *ab initio* wave functions used in the interpretation of parity nonconservation experiments in the cesium atom. While a number of accurate lifetime values have recently appeared in the literature for the  $6P$  states, our absorption measurements provide an independent measure of the *relative* transition strengths with much higher precision. Further, the  $6^2S_{1/2}$ - $6^2P_J$  line strengths are already known from the lifetime measurements to better than 0.25%, and may be used to calibrate the measurement of transitions to poorly known levels which are accessible from the ground state. Of particular interest are the  $6^2S_{1/2}$ - $7^2P_J$  electric dipole amplitudes and the  $6^2S_{1/2}$ - $7^2S_{1/2}$  Stark-induced transition amplitudes. The latter quantities are of special significance, because the lack of empirical knowledge of these Stark polarizabilities is presently the limiting factor in extracting fundamental weak interaction parameters from the most precise atomic parity nonconservation measurements [1,2].

The absorption spectrometer described in this work has an intensity resolution of 0.04% and a frequency resolution of  $\approx 1$  MHz maintained over several GHz of detuning. As will be demonstrated, this is sufficient to determine in a single measurement the column absorbance of the vapor with a precision of  $\approx 0.06\%$  when combined with a suitably accurate model of the absorption line profile. This paper is divided into four sections. Section I outlines the theoretical background and line shape model used in the interpretation of the results. Section II describes the experimental apparatus and quantifies its resolving power. Section III reports the results of a measurement of the ratio of the  $6S$ - $6P_J$  transition strengths to a precision of 4.5 parts in  $10^4$  along with a detailed analysis of error contributions. The final section

compares the results with other experiments and theory, and offers some general comments on possibilities for future measurements.

### II. BACKGROUND AND LINE SHAPE MODEL

#### A. Propagation of light in a polarizable medium

Our experiment is based on the careful measurement of the frequency-dependent transmission of an atomic cesium vapor. In order to extract the probability for photon absorption by individual atoms from such a measurement, it is necessary to have a model which relates the observed spectra to various fundamental quantities such as transition matrix elements, linewidths, and vapor densities. The macroscopic wave equation

$$-\nabla^2 \vec{E} + \mu \frac{\partial \vec{J}}{\partial t} + \frac{1}{c^2} \frac{\partial^2 \vec{E}}{\partial t^2} = -\mu \frac{\partial^2 \vec{P}}{\partial t^2} \quad (1)$$

governs the propagation of light as it interacts with a medium of polarizability  $\vec{P}$  embedded in a host medium with speed  $c = 1/\sqrt{\mu\epsilon}$ . In the limit of slowly varying electric field amplitude and phase, the wave equation can be decomposed into two first-order equations [3]

$$\frac{\partial \mathcal{E}}{\partial z} + \frac{1}{c} \frac{\partial \mathcal{E}}{\partial t} = -\frac{k}{2\epsilon} \text{Im}(\mathcal{P}), \quad (2a)$$

$$\mathcal{E} \left( \frac{\partial \phi}{\partial z} + \frac{1}{c} \frac{\partial \phi}{\partial t} \right) = -\frac{k}{2\epsilon} \text{Re}(\mathcal{P}), \quad (2b)$$

where  $k$  is the electromagnetic wave vector, and for convenience the electric field and polarization have been decomposed into positive and negative frequency parts

$$\vec{E} = \mathcal{E} \hat{e} e^{i(kz - \omega t - \phi)} + \text{c.c.}, \quad (3a)$$

$$\vec{P} = \mathcal{P} \hat{e} e^{i(kz - \omega t - \phi)} + \text{c.c.} \quad (3b)$$

The field amplitude  $\mathcal{E}$  can be taken to be a real quantity without loss of generality (imaginary parts can be absorbed

\*Present address: Time and Frequency Division, National Institute of Standards and Technology, 325 Broadway, Boulder, CO 80303.

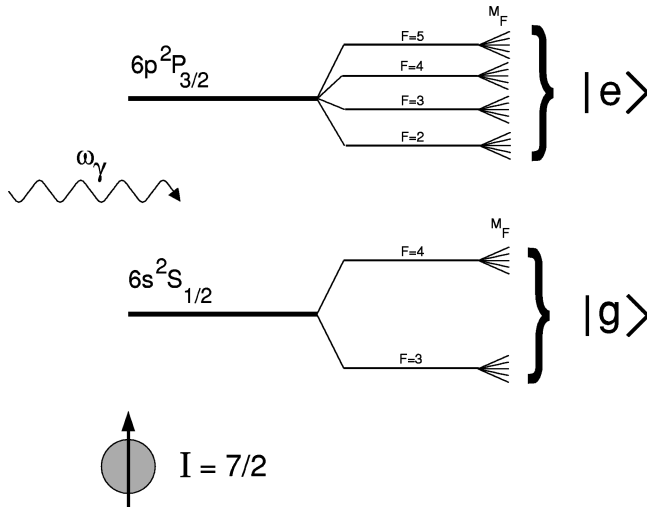


FIG. 1. Electronic state schematic for modeling of absorption line shape,  $J=3/2$  case shown.

into the unit vectors  $\hat{\epsilon}$  or the phase  $\phi$ ). The polarization amplitude is typically complex, and shares the same time dependence as the field amplitude apart from phase lags. The polarization amplitude which appears in the medium upon application of an external field is linearly related to the field amplitude (for values of the Rabi frequency much less than the spontaneous emission rate  $\vec{E} \cdot \vec{D} \ll \Gamma_e$ ), i.e.,

$$\mathcal{P} = A \mathcal{E}, \quad (4)$$

where  $A$  is a complex quantity. Using this condition and further restricting the analysis to the case of a constant field envelope ( $\partial \mathcal{E} / \partial t = 0$ ), Eq. (2a) can be directly integrated to yield the electric field amplitude after traversing a length  $z$  of the medium

$$\mathcal{E}(z) = \mathcal{E}_0 e^{-(k/2\epsilon)\text{Im}(A)z}, \quad (5)$$

which is the familiar Bouguier-Lambert-Beer expression for field attenuation in a medium with complex amplitude absorption coefficient  $A$ . The problem is therefore one of calculating the coefficient  $A$ , or equivalently, the complex polarizability  $\mathcal{P}$  for near-resonant light propagating in an atomic cesium vapor.

### B. Polarizability of an atomic vapor

Consider the system depicted in Fig. 1, consisting of a single atom in a continuous-wave laser field of frequency  $\omega_\gamma$  and having unresolved or partially resolved hyperfine structure and unresolved magnetic sublevels. Let  $e$  and  $g$  label states in the excited- and ground-state manifolds, respectively, with energies  $\hbar\omega_e$ ,  $\hbar\omega_g$ , and separations  $\omega_{eg} = \omega_e - \omega_g$ . In general, the atom will be found in a superposition of excited and ground states  $\psi$  such that

$$|\psi\rangle = \sum_g a_g |g\rangle e^{-i\omega_g t} + \sum_e b_e |e\rangle e^{-i\omega_e t}. \quad (6)$$

$|g\rangle$  and  $|e\rangle$  are eigenfunctions of the atomic Hamiltonian including hyperfine interactions and hyperfine Zeeman terms (if any). The atom-field interaction is treated as a perturba-

tion; from first-order time-dependent perturbation theory, the equation of motion for the excited-state amplitudes  $b_e$  is

$$i\hbar \dot{b}_e = \sum_g \langle e | \mathcal{V} | g \rangle a_g e^{i\omega_{eg} t} - i\hbar \frac{\Gamma_e}{2} b_e. \quad (7)$$

The atom-field interaction  $\mathcal{V}$  is simply  $e\vec{E} \cdot \vec{r} = -\vec{E} \cdot \vec{D}$ , and a phenomenological damping term has been added to account for decay of the excited-state population (which may include processes other than spontaneous emission of a photon). Decomposing the laser electric field into a coherent superposition of plane waves,

$$\vec{E}(t) = \vec{\mathcal{E}} e^{-i\omega_\gamma t} + \vec{\mathcal{E}}^* e^{+i\omega_\gamma t}, \quad (8)$$

one easily obtains from these equations the low-intensity steady-state dipole moment induced by the field  $\vec{E}(t)$ :

$$\begin{aligned} \langle \vec{D} \rangle &= \langle \psi | \vec{D} | \psi \rangle \\ &= \sum_e \sum_{g,g'} a_{g'}^* a_g \frac{(\vec{\mathcal{E}}^* \cdot \vec{D}_{g'e}) e^{-i(\omega_{eg'} - \omega_\gamma)t}}{\hbar(\omega_{eg'} - \omega_\gamma) + i\hbar \Gamma_e/2} e^{i\omega_{eg} t} \vec{D}_{eg} \\ &\quad + \sum_e \sum_{g,g''} a_g^* a_{g''} \frac{(\vec{\mathcal{E}} \cdot \vec{D}_{eg''}) e^{+i(\omega_{eg''} - \omega_\gamma)t}}{\hbar(\omega_{eg''} - \omega_\gamma) - i\hbar \Gamma_e/2} e^{i\omega_{eg} t} \vec{D}_{ge}, \end{aligned} \quad (9)$$

where unobservable contributions which oscillate at optical frequencies have been discarded (rotating wave approximation), and we introduce a shorthand for the dipole matrix element  $\vec{D}_{eg} = \langle e | \vec{D} | g \rangle$ . The terms  $a_i^* a_j$  are identified with the elements  $\rho_{ij}$  of the density matrix which describes a statistical mixture of the ground-state amplitudes. For the purposes of the present experiment, we can make the simplifying assumption of no optical pumping (see Sec. III) and assign the ground state a thermal population distribution

$$a_i^* a_j \equiv \rho_{ij} = \frac{1}{g_j} \delta_{ij},$$

where  $g_j$  is the appropriate (ground-) state degeneracy. The elimination of coherences from the density matrix simplifies the sums, and the induced dipole moment becomes

$$\begin{aligned} \langle \vec{D} \rangle &= \frac{1}{\hbar} \sum_{eg} \frac{1}{g_g} \left\{ \frac{(\vec{\mathcal{E}}^* \cdot \vec{D}_{ge}) \vec{D}_{eg} e^{+i\omega_\gamma t}}{(\omega_{eg} - \omega_\gamma) + i\Gamma_e/2} \right. \\ &\quad \left. + \frac{(\vec{\mathcal{E}} \cdot \vec{D}_{eg}) \vec{D}_{ge} e^{-i\omega_\gamma t}}{(\omega_{eg} - \omega_\gamma) - i\Gamma_e/2} \right\}. \end{aligned} \quad (10)$$

We now evaluate  $\langle \vec{D} \rangle$  for positive (left-circularly polarized) and negative (right-circularly polarized) helicity light via substitution of the appropriate fields  $\vec{\mathcal{E}}_\pm$ ,

$$\vec{\mathcal{E}}_\pm = \mp \frac{E_0}{\sqrt{2}} e^{ik \cdot \vec{x}} \hat{e}_\pm,$$

where  $E_0$  is the field strength and the  $\hat{e}_\pm = \mp(\hat{x} \pm i\hat{y})/\sqrt{2}$  are spherical unit vectors. Decomposing  $\langle \vec{D} \rangle$  as we have done for  $\vec{\mathcal{E}}$ ,

$$\langle \vec{D} \rangle = \vec{D} e^{-i\omega_\gamma t} + \vec{D}^* e^{+i\omega_\gamma t},$$

the induced dipole moments are found to have complex dipole amplitudes  $\vec{D}_\pm$ , where the subscript indicates the result for driving fields of either positive or negative helicity:

$$\vec{D}_\pm = \frac{e^2}{\hbar} \left\{ \sum_{eg} \frac{1}{g_g} \frac{|e|r_\pm|g\rangle|^2}{(\omega_{eg} - \omega_\gamma)^2 + \Gamma_e^2/4} \times \left( \omega_{eg} - \omega_\gamma + i \frac{\Gamma_e}{2} \right) \right\} \vec{\mathcal{E}}_\pm. \quad (11)$$

For clarity and further computation,  $\vec{D}_{ge}$  is written here as a radial matrix element of the appropriate spherical component.

### C. Absorption coefficient

Application of the results of Eqs. (4) and (5) yields the electric field attenuation coefficient

$$\begin{aligned} \alpha_\pm &= \frac{k}{2\epsilon_0} \text{Im}(A) \\ &= 2\pi\alpha \frac{\hbar\omega_\gamma}{e^2} \text{Im} \left( \frac{n\mathcal{D}_\pm}{\mathcal{E}_\pm} \right) \\ &= n\pi\alpha\omega_\gamma \sum_{eg} \frac{\Gamma_e}{g_g} \frac{|e|r_\pm|g\rangle|^2}{(\omega_{eg} - \omega_\gamma)^2 + \Gamma_e^2/4}, \end{aligned} \quad (12)$$

where  $n$  is the number density of atoms in the vapor and  $\alpha$  is the fine structure constant  $e^2/4\pi\sigma_0\hbar c$ ; the macroscopic volume polarizability is directly related to the microscopic dipole moment by  $\vec{P} = n\langle \vec{D} \rangle$ .

Finally, it is necessary to include the inhomogeneous broadening due to thermal motion of the atoms in the vapor. Since the atomic polarizability is calculated for an atom at rest, we must Doppler shift the laser frequency  $\omega_\gamma$  to its proper value in the atomic frame. Integration over the Maxwell velocity distribution for a gas of cesium atoms with atomic mass  $M$  and equilibrium temperature  $T$  yields

$$\begin{aligned} \alpha_\pm &= n\pi\alpha\omega_\gamma \sqrt{\frac{M}{2\pi kT}} \sum_{eg} \left\{ \frac{\Gamma_e}{g_g} |e|r_\pm|g\rangle|^2 \right. \\ &\quad \left. \times \int_{-\infty}^{\infty} \frac{e^{-Mv^2/2kT} dv}{[\omega_\gamma(1-v/c) - \omega_{eg}]^2 + \Gamma_e^2/4} \right\}, \end{aligned} \quad (13)$$

where  $k$  is the Boltzmann constant. Because the inhomogeneous width is narrower than both the cesium ground-state and  $6^2P_{1/2}$  excited-state hyperfine splittings, the total angular momentum basis  $|F, M_F\rangle$  is convenient for evaluation of the absorption. Applying the Wigner-Eckhart theorem and separating the electronic and nuclear variables, we arrive at the basic result of this section:

$$\begin{aligned} \alpha_\pm &= \frac{n\pi\alpha\omega_\gamma}{(2I+1)(2J_g+1)} \sqrt{\frac{M}{2\pi kT}} | \langle J_e || \vec{r} || J_g \rangle |^2 \\ &\quad \times \sum_{F_e M_e} \sum_{F_g M_g} (-1)^{2(I+J_e-M_e)} (2F_e+1)(2F_g+1) \\ &\quad \times \left( \begin{array}{ccc} F_e & 1 & F_g \\ -M_e & \pm 1 & M_g \end{array} \right)^2 \left\{ \begin{array}{ccc} J_e & F_e & I \\ F_g & J_g & 1 \end{array} \right\}^2 \\ &\quad \times \int_{-\infty}^{\infty} \frac{\Gamma_e e^{-Mv^2/2kT} dv}{[\omega_\gamma(1-v/c) - \omega_{F_e M_e F_g M_g}]^2 + \Gamma_e^2/4}. \end{aligned} \quad (14)$$

The transmitted intensity for the linearly polarized light used in the experiment is obtained by writing its electric field in the spherical basis and using Eq. (5) to find the attenuation of each helicity component. After propagation through a vapor of length  $z$ , the resultant transmitted intensity fraction for linearly polarized light is found in this fashion to be

$$T(z) = \frac{I(z)}{I(0)} = \frac{1}{2} (e^{-2\alpha_+ z} + e^{-2\alpha_- z}). \quad (15)$$

In the case of zero magnetic field,  $\alpha_+ = \alpha_-$  (and there is similarly no phase shift of the electric field). The computer code employed for the analysis is capable of diagonalizing the atomic Hamiltonian in an external magnetic field using the hyperfine basis, and in fact computes the different coefficients and resulting phase shifts. This allows us to properly model magneto-optic effects (birefringence, optical rotation) in the vapor.

Some comments concerning the fitting procedure are in order. Any iterative fitting scheme (we use a modified Levenberg-Marquardt method [4]) requires many repeated evaluations of Eq. (15) with small variations in the undetermined parameters which we hope to extract from the fit. The Voigt profile integral of the Doppler-broadened radiative line is the primary bottleneck in any such procedure, because brute-force evaluation at the required accuracy is costly in terms of computer resources. Fortunately, there exist a number of methods for simplified evaluation of integrals of this type. A computationally efficient and very accurate power series approximation is given by Chiarella and Reichel [5]. We use their method and recurrence relations to compute the integral and curvatures, obtaining an accuracy of 4.8 parts in  $10^9$  when retaining nine terms of the series. Fitting is carried out on a high-performance RISC workstation, and a typical scan of 2000 laser frequency channels takes one to two hours to converge.

### III. APPARATUS

The spectrometer consists of a scanning single-frequency Ti:sapphire laser, the output of which is stabilized and split into probe and reference beams (both of 100–200 nW/cm<sup>2</sup> intensity) which are used to probe the transmission of a quartz cell containing cesium vapor (Fig. 2) with a 2.25 cm optical path length. The probe and reference signals are detected with a matched pair of silicon photodiodes and recorded under computer control. The apparatus is described in great detail elsewhere [6]; only the most important features are sketched in this paper.

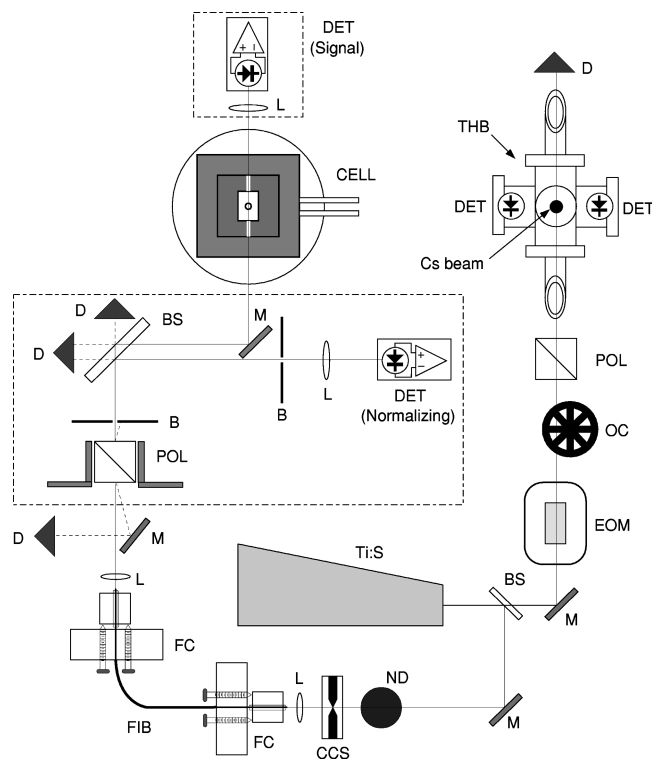


FIG. 2. Schematic of apparatus and optical path. Legend: Ti:S, Ti:sapphire laser; BS, beam splitter; *M*, gold first-surface mirror; ND, neutral density filter; CCS, computer-controlled shutter; *L*, lens; FC, fiber coupler and alignment stage; FIB, single-mode fiber; *D*, light dump; POL, linear polarizer; *B*, large baffle; CELL, cell in oven; DET photodiode detector; EOM, electro-optic modulator in resonant cavity; OC, optical chopper, and THB, cesium thermal beam apparatus. Dotted lines indicate light-tight enclosures, drift tubes omitted for clarity.

The most significant obstacles to high-precision absorption measurements in an apparatus of this type are pointing stabilization of probe light, maintenance of the normalization integrity, and control of the vapor density. The use of a ring laser introduces output pointing instabilities because as the frequency of laser oscillation is tuned by manipulation of various dispersive elements in the cavity (Brewster plates, étalons, etc.), the output beam is either displaced or tilted slightly with respect to the initial condition. When multiplied by a long optical lever arm, such wandering of the beam can have significant impact on intensity normalization and lead to changes of the optical path length in the vapor. We overcome the pointing limitations by employing a single-mode optical fiber and various coupling optics as a spatial filter. The fiber output is free from measurable position and angle fluctuations even for maximal excursions of the ring cavity optics (i.e., beyond which the laser ceases to operate).

The accuracy of the probe-to-reference normalization can be compromised by pointing instabilities, interference effects, unwanted scattered light, and data acquisition limitations. The optical path is constrained by the fiber and completely enclosed in drift tubes to decrease any instability due to convective refraction effects during propagation in air. Interference effects are minimized by mounting the spectrometer elements on micrometer tilt and rotation stages, and the incidence angles are carefully adjusted to reduce any

modulation to below the detection limits of the apparatus. Much of the challenge in obtaining accurate absorption spectra lies in the control of unwanted scatter from sources both internal and external to the spectrometer's optical elements, and many diagnostics were found to be necessary to identify and control the various background sources. Because of the high intensity of the scatter produced far upstream near the laser source, even small light leaks show up on the detector, usually as frequency-dependent effects. Inside the spectrometer enclosure, waste light from inside the polarizer, and back reflections from the beam splitter, cell windows, and focusing lenses are the major culprits. This scatter is eliminated through the judicious use of absorptive baffles and shields, along with limiting apertures which block diffraction haloes. In its final configuration, all sources of extraneous scatter are identified and eliminated to the technical limits of detection in the apparatus (better than 0.05% relative intensity).

Two matched silicon photodiodes (responsivity 0.5 A/W) detect the probe and reference beams. These photocurrents are converted to voltages using identically constructed current to voltage amplifiers. Identical gated integrators of our own design integrate these voltages for about 17 ms, then hold the final values for reading by an analog-to-digital converter. We choose the gain of the detection system to produce signals of a one volt at the input to the analog to digital converter for an input power of about 80 nW. Our data acquisition system consists of four identical gated integrators which permit the simultaneous collection of four detector signals. The third integrated photosignal comes from the atomic beam tube fluorescence which is used to calibrate the laser frequency scan as described later in this paper. The fourth is used for a variety of diagnostic purposes. All four signals are sampled and recorded simultaneously even though the analog-to-digital conversion must be performed sequentially; otherwise laser power fluctuations on a time scale of tens of milliseconds could destroy the integrity of the normalization process. In addition a shutter blocks and unblocks the laser under computer control so that instrumental voltage offsets can be recorded and subtracted from all signals. Each absorption data point consists of the integrated probe signal voltage minus its integrated offset voltage, divided by the integrated reference signal voltage minus its integrated offset voltage. With this normalization scheme, the detector efficiencies and conversion gains divide out yielding the intensity ratio of the probe to reference beams. Any remaining differences in gain or efficiency between these two data channels results in an overall scaling factor that does not affect our result because the analysis depends solely on the fractional size of the absorption.

The quartz cell consists of a cylindrical body 2.5 cm in diameter and 2.25 cm long. A narrow sidearm extends downward from the center of the body. The probe laser beam passes through fused silica windows which cover both ends of the cylindrical body. The sidearm contains cesium in the lowest 1 cm of its 9.5 cm length. The cell is evacuated with an oil-free system including an ion pump and baked until the pressure reaches a value of less than  $10^{-6}$  Pa. Cesium is distilled into the sidearm from an ampoule containing better than 99.9% pure Cs<sup>133</sup>. No coatings or buffer gases are added to the cell, and any residual gas is expected to have atmospheric ratios. At these pressures we expect little for-

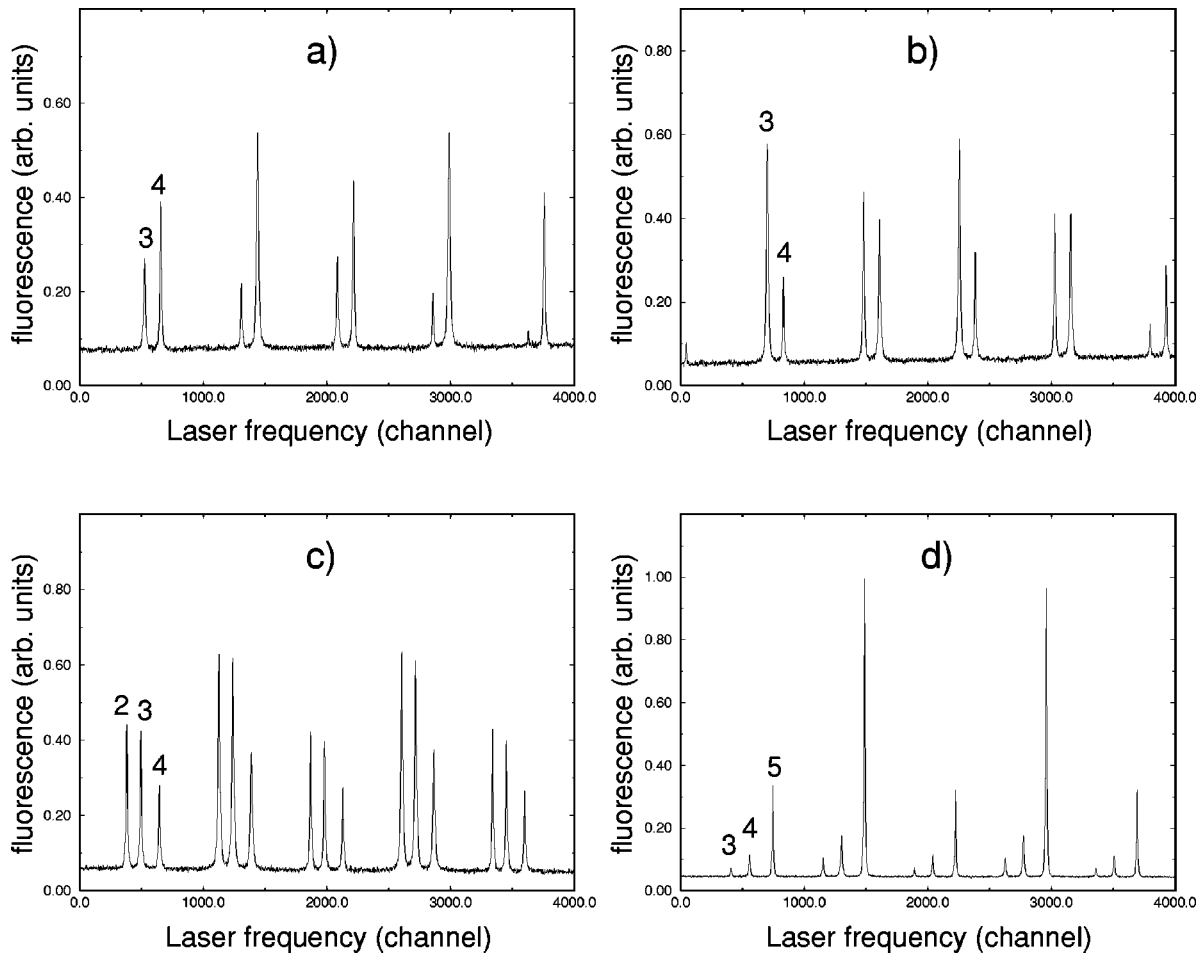


FIG. 3. 1-GHz optical phase-modulated thermal beam spectra. Vertical axis is fluorescence intensity (arbitrary units), horizontal is laser frequency step number. The four possible cases are shown: (a)  $6^2S_{1/2}F=3 \rightarrow 6^2P_{1/2}F'=3,4$ ; (b)  $6^2S_{1/2}F=4 \rightarrow 6^2P_{1/2}F'=3,4$ ; (c)  $6^2S_{1/2}F=3 \rightarrow 6^2P_{3/2}F'=2,3,4$ ; (d)  $6^2S_{1/2}F=3 \rightarrow 6^2P_{3/2}F'=3,4,5$ .

eign gas broadening and the collisional linewidths observed are consistent with pure resonance broadening (Cs on Cs).

In order to make a meaningful comparison of the absorption on two different transitions, the vapor density in the cell must be held constant during the entire observation period. At present, this includes the time required to retune the laser from operation at 852 nm to 894 nm. In the future, two lasers will reduce the time between measurements. To maintain a constant density over time, the vapor cell is contained in a temperature controlled enclosure consisting of two parts: an oven for the cell body, and a second oven for the lowest 1 cm of the descending sidearm. Because the vapor pressure is determined by the temperature of the condensate in the coldest region of the cell, we employ two precise temperature servos which are capable of stabilizing the cell and stem temperatures separately to  $\pm 5$  mK for periods of several hours. A gradient of 10–15 K is usually maintained between the two ovens to prevent condensation in the cell volume. For measurements performed below the freezing point of cesium (301.55 K), it was necessary to keep the cell body above the freezing point to stabilize the density and provide repeatable results; the temperature gradients were correspondingly greater under these circumstances.

Laser frequency calibration during the sweeps [7,8] is accomplished by probing a cesium thermal beam with 1 GHz phase-modulated light [9]. Approximately 5 W of micro-

wave power are coupled into a resonant-cavity type electro-optic modulator (EOM), and the depth of modulation is tuned such that useful light power densities appear in the zeroth-, first-, second-, and third-order sidebands. As the laser is scanned through the resonance transition in the vapor cell, the phase-modulated light excites the atomic beam, and the beam resonance fluorescence is detected using two silicon photodiodes. We employ phase-sensitive detection of the fluorescence signal using a lock-in amplifier; the lock-in output is recorded as a function of the voltage used to scan the Ti:sapphire laser frequency. The thermal beam signal exhibits well-defined peaks [full width at half maximum (FWHM)  $< 35$  MHz] corresponding to excitation to various upper-state hyperfine levels, which repeat every 1 GHz interval as the successive sidebands sweep through resonance. Figure 3 shows typical thermal beam calibration spectra for the four cases of interest. The group-to-group separation is determined solely by the drive frequency of the EOM, which is measured with a frequency counter to a precision of 1 kHz. The peak spacing within the hyperfine groups is known with a precision of 320 kHz in the case of the  $6^2P_{1/2}$  [9], and to 20 kHz in the case of the  $6^2P_{3/2}$  [10] from independent measurements. Hence the complete spectrum can be used to generate an extremely accurate calibration of the laser frequency which requires no external stabilization and exhibits unparalleled long term stability and repeatability.

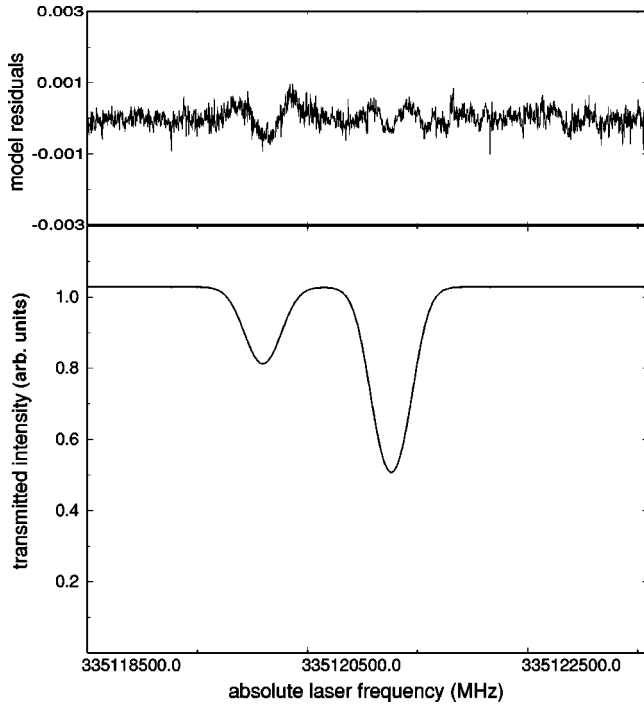


FIG. 4. Transmission near the  $6^2S_{1/2}F=3 \rightarrow 6^2P_{1/2}F'$  line center. Vertical axis is normalized transmission (arbitrary units), plotted against the laser frequency extracted from a concurrently measured thermal beam spectrum. Upper plot shows residuals of best fit to model, which has  $nS(6^2P_{1/2})=0.2377 \times 10^{-2} \text{ m}^{-1}$ . Stem temperature is 318.658(5) K.

#### IV. EXPERIMENT AND RESULTS

Absorption spectra are collected under computer control by scanning the laser over the resonance lines, with total detunings ranging from  $\pm 2.5$  to  $\pm 3.5$  GHz depending on the Doppler width. For the present investigation, 32  $D1$  and 37  $D2$  absorption spectra are acquired and fit to the line shape model of Sec. II. In general, we use the smallest detuning range possible to obtain the greatest resolution from our acquisition system which has 4000 laser frequency bins, although we are careful to acquire transmission information in the very far wings (where the absorption is negligibly small) so that the incident intensity can be independently calibrated. Due to the narrowness of the scans, we measure excitation from each of the ground-state hyperfine levels separately. Fitting these two transitions independently also provides a convenient test of line shape model systematics which may be dependent on the relative strengths of the unresolved upper-state hyperfine components (e.g., optical pumping and collisional processes). We typically obtain four scans for a single fine structure component, consisting of two repeated scans each over the transitions from  $6^2S_{1/2} F=3$  and  $F=4$  to  $6^2P_J F'$  states. Subsequently, the laser is tuned to the other fine structure component and the same group of measurements is performed. We then change the temperature/density, allow the system to equilibrate at the new temperature for several hours, and repeat the measurement procedure to check for systematics which are temperature or density dependent. Various diagnostic tests are also performed, which include switching back and forth between the  $D1$  and  $D2$  lines repeatedly at fixed temperature, and measuring the

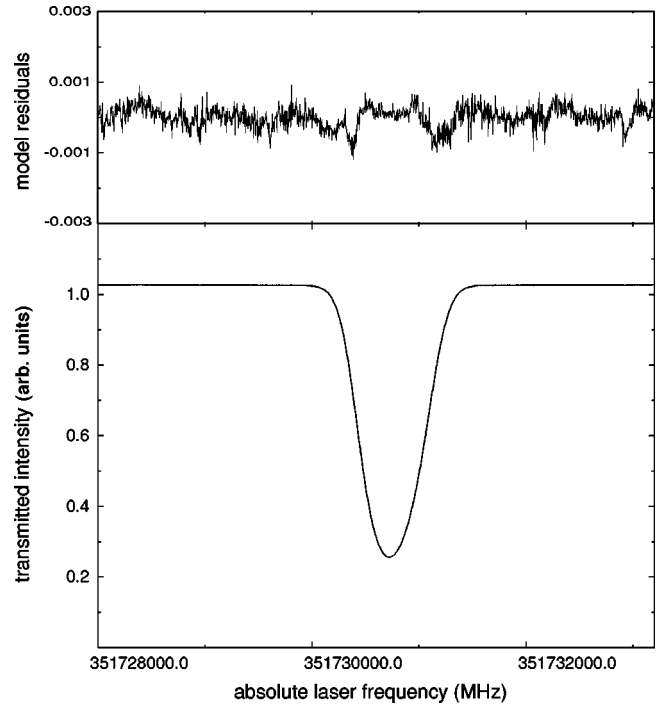


FIG. 5. Transmission near the  $6^2S_{1/2}F=3 \rightarrow 6^2P_{3/2}F'$  line center. Vertical axis is normalized transmission (arbitrary units), plotted against the laser frequency extracted from a concurrently measured thermal beam spectrum. Upper plot shows residuals of best fit to model, which has  $nS(6^2P_{3/2})=0.4707 \times 10^{-2} \text{ m}^{-1}$ . Stem temperature is 318.644(5) K.

absorption on a single line every five minutes for an hour to check the maintenance of equilibrium. Figures 4 and 5 show representative absorption spectra after the frequency scale has been calibrated using the thermal beam reference, along with the residual differences between the measured transmission and the model. The residual deviations that appear larger than the intensity noise originate from statistical uncertainties in determining the horizontal frequency scale from the beam-tube spectra (Fig. 3). When averaged over several scans under the same conditions these residuals average to zero. The data are fit to the line shape model [Eqs. (14) and (15)] with three undetermined parameters: a small frequency offset to  $\omega_\gamma$ , the normalized incident intensity, and the parameter of interest  $nzS$  where  $S$  is the line strength  $\langle J_e || \vec{r} || J_g \rangle^2$ . The ratio of the  $D1$  and  $D2$  line strengths can then be found from the ratio of the two  $nzS$  measurements. Because the column length  $z$  is well defined and fixed in our apparatus, we will factor it out in the foregoing discussion. At constant temperature the densities  $n$  cancel, and

$$\mathcal{R} = \frac{nS(D2)}{nS(D1)} = \frac{S(D2)}{S(D1)} = \frac{\langle 6p^2P_{3/2} || \vec{r} || 6s^2S_{1/2} \rangle^2}{\langle 6p^2P_{1/2} || \vec{r} || 6s^2S_{1/2} \rangle^2}. \quad (16)$$

Uncertainty in extracting the value of  $nS(6P_J)$  from the absorption measurements arises from the statistical error in the fitting process, and from systematic error in the model parameters corresponding to the Lorentzian linewidth and vapor kinetic temperature. Technical noise in the transmitted light is approximately constant for all points across the spec-

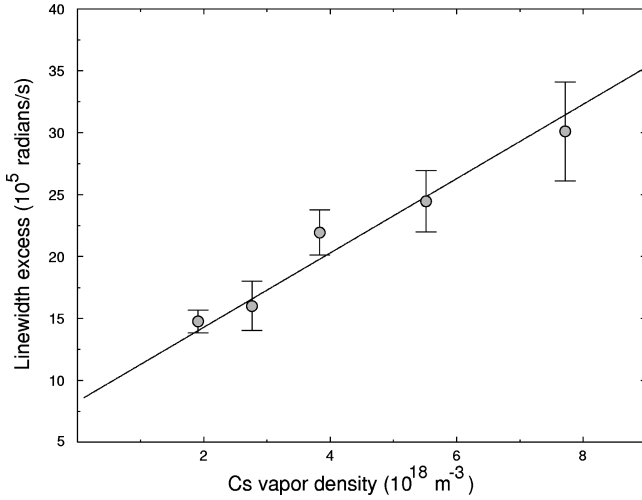


FIG. 6. Excess linewidth beyond natural value, extracted from high-density absorption spectra. Error bars represent standard error in repeated measurement. The line is the best linear fit to the data, with slope of  $3.0(5) \times 10^{-13}$  radians  $\text{m}^3/\text{s}$  and intercept of  $9(2) \times 10^5$  radians/s.

tra, at the level of 0.04% of the incident intensity. A comparatively large uncertainty appears in the normalization of the light power because of the limited resolution of the analog-to-digital converters used in recording the spectra. In both the signal and reference channels, the instrumental voltage offsets are subtracted by shuttering the laser. The offsets cannot be measured to better than 0.018% in our 12-bit converter; this is equivalent to a 0.025% uncertainty in the transmitted intensity at all points on the spectrum.

The largest contribution to the uncertainty in determining  $nS$  from the individual fits comes from lack of knowledge of the Lorentzian width of the Voigt profile. In the real case of a probe laser source with finite bandwidth, this includes the laser linewidth as well as the upper-state population damping rate. In the limit of zero density, radiative damping at the spontaneous emission rate is exact, but at higher densities, collisional processes deplete the excited-state population at enhanced rates. To determine the rate constant  $\Gamma_e$  for decay of the excited state, we increase the density so that essentially no light is transmitted to the detector for detunings of several hundred MHz around the  $6^2P_{3/2}$  line center, which improves our sensitivity to the Lorentzian contribution to the profile. We are then able to extract the collisional linewidth with some precision by fitting these spectra with the damping rate as a free parameter. Within the present limitations of our experiment, we find agreement with the impact-regime resonance broadening calculations of Carrington, Stacey, and Cooper [11], who predict that the collisional depopulation rate of the  $6^2P_{3/2}$  state increases linearly with the vapor density, with a slope of  $3.29 \times 10^{-13}$  radians  $\text{m}^3/\text{s}$ . The best fit to our linewidth data for densities between  $10^{18}$  and  $10^{19}$   $\text{m}^{-3}$  returns a slope of  $3.0(5) \times 10^{-13}$  radians  $\text{m}^3/\text{s}$  (Fig. 6). For absorption to the  $6^2P_{1/2}$  state we did not perform the high-density linewidth measurement. Because we find good agreement with the impact calculation for the  $D2$  transition, we believe that the theoretical prediction for the  $D1$  transition is similarly robust.

In the lower-density regime where absorption measurements for the ratio experiment are actually performed, we are not able to directly distinguish between radiative and total collisional linewidths due to the statistical insensitivity of the fit to the Lorentzian part of the profile. Important information can, however, still be obtained by observing trends in all of the data sets taken as a whole. A simple test involves comparing the Doppler linewidth inferred from the fit with that expected from the temperature of the vapor. The total linewidth is a combination of our best estimate of a 500-kHz laser width, plus the best fit linewidth for the  $D2$  transition and impact linewidths for the  $D1$  transition. Taking into account the small (1.75 G) magnetic field present due to the optical table and heaters as well, we fit all spectra with the kinetic temperature of the vapor floating as a free parameter. In this case, the difference  $\Delta T$  between fitted and measured vapor temperatures for all data takes the mean value  $\langle \Delta T \rangle = 0.12(17)$ , which is consistent with zero. If the laser linewidth and magnetic field are not included in the model, we find  $\langle \Delta T \rangle = 0.75(17)$ , which indicates a deficiency in the calculated width of the profile. We believe that with the addition of contributions for the collisional, laser, and magnetic field effects, the total Lorentzian linewidth is accurate to within a few hundred kHz for both the  $D1$  and  $D2$  transitions. The best linear fit to the collisional width data (Fig. 6), which demonstrates excellent agreement with the slope predicted in the impact regime [11], returns an intercept of 150(30) kHz when extrapolated to zero density. This is inconsistent with the expected residual linewidth due to the laser, which should yield an intercept of approximately 500 kHz as stated by the manufacturer. We take this discrepancy as the uncertainty in our knowledge of the Lorentzian contribution to the  $6^2P_{3/2}$  linewidth, which is equal to 6% of the total damping rate. An identical estimate of 6% uncertainty is made for the  $6^2P_{1/2}$  width. Geometric considerations lead to a  $6^2P_{1/2}$  collisional damping rate which is  $\approx 2/3$  that of the  $6^2P_{3/2}$  level, so we feel that this second uncertainty estimate is conservative even without a direct measurement for the  $D1$  line.

To determine the dependence of the desired quantities  $nS(6^2P_j)$  on the uncertainty in the Lorentzian width, simulated data with known linewidths and temperatures are fit with fixed, discrepant values of said linewidth. For perhaps more realistic tests, we also vary the linewidths in fits to all of the actual data and determine the relationship between the Lorentzian width and the fitted values of  $nS(6^2P_j)$ . Both methods produce consistent behavior. The variation in  $nS(6^2P_j)$  is approximately linear with respect to changes in the damping rate, even for extremely large excursions (up to  $\approx 60\%$  of the radiative value). This reflects the insensitivity of the model to the collisional contribution to the Voigt profile at the low densities used for the ratio measurement. Note that this represents the average behavior for a range of optical depths; however, the variation is relatively constant for the densities used in the ratio measurement [6]. In this manner we determine the following dependences:

$$\frac{\Delta[nS(6^2P_{1/2})]}{nS(6^2P_{1/2})} = 9.1 \times 10^{-3} \frac{\Delta\Gamma_e}{\Gamma_e}, \quad (17)$$

$$\frac{\Delta[nS(6^2P_{3/2})]}{nS(6^2P_{3/2})} = 6.0 \times 10^{-3} \frac{\Delta\Gamma_e}{\Gamma_e}.$$

Using the 6% linewidth uncertainty in each case, we arrive at a systematic uncertainty in the column density-line strength product of 0.055% and 0.036% for the  $D1$  and  $D2$  transitions, respectively.

Because the experiment is performed in the Doppler-broadened regime, accurate characterization of the kinetic temperature of the vapor is required to make comparisons with the theoretical line profile. Four-wire resistance measurements of platinum resistive temperature device (RTD) thermometers embedded in the ovens provide the cell body and stem temperatures with a resolution of  $\pm 1$  mK; we expect that as an absolute measurement of temperature the accuracy is worse by not more than about a factor of 5. Relative temperature measurements using thermocouples placed at various points on the cell oven indicate that the temperature of the cell body is uniform to better than the limited precision of 100 mK achieved using this technique. We take 100 mK as the maximum uncertainty in the absolute temperature at any point in the cell oven volume. The nonequilibrium nature of the apparatus (cell body and Cs-containing stem at temperatures differing by 10 to 20 K) is not anticipated to introduce significant deviations from the Maxwellian velocity distribution. Other work employing a similar apparatus using Rb vapor demonstrates excellent agreement between measured cell temperatures and fitted Maxwellian Doppler line profiles, even for cell-stem temperature differences of 200 K [12].

The systematic effects of uncertainty in the kinetic temperature are determined in a manner identical to that used for the Lorentzian width, by fitting simulated spectra with known but discrepant temperatures, and via a variational technique in which the input temperatures of all the real data sets are varied and the change of the column density-line strength product  $nS(6^2P_J)$  is recorded. Both techniques give consistent variations, with the following dependences:

$$\frac{\Delta[nS(6^2P_{1/2})]}{nS(6^2P_{1/2})} = 8 \times 10^{-4} \frac{\Delta T_{\text{kinetic}}}{T_{\text{kinetic}}},$$

$$\frac{\Delta[nS(6^2P_{3/2})]}{nS(6^2P_{3/2})} = 3 \times 10^{-5} \frac{\Delta T_{\text{kinetic}}}{T_{\text{kinetic}}}.$$

Again, the dependence is found to be relatively constant for the range of optical depths under consideration; the preceding values represent the average behavior. Consequently, the typical uncertainty of 0.1 K in the kinetic temperature of the vapor corresponds to an uncertainty in the density-line strength product of 0.008% for absorption near the  $D1$  line, and 0.003% for absorption near the  $D2$  line.

Noise originating in the detection and acquisition system contributes a random uncertainty in the measured absorption of  $\approx 0.04\%$  of the total incident intensity, and there is a relative frequency uncertainty of  $\pm 1$  laser channel arising from the finite width of the peaks in the beam-tube spectrum. These uncertainties are considered in the fitting procedure. Reduced  $\chi^2$  values for all fits with the instrumental offsets properly subtracted fall in the interval from 0.25 to 3.6, with almost all fits consistently near  $\chi^2 = 0.4$ , which is the expected distribution. Statistical uncertainties in the parameters of interest are determined via the full covariance matrix output by the fitting routine, which returns the variation in  $\chi^2$  near the minimum value. The  $1\sigma$  confidence interval is de-

TABLE I. Summary of error contributions for individual absorption measurements.

Error term	$\sigma[nzS(6P_{1/2})]$	$\sigma[nzS(6P_{3/2})]$
ADC accuracy in offset	0.025%	0.025%
Lorentzian width	0.055%	0.036%
Vapor kinetic temperature	0.008%	0.003%
Statistical error in fitting	$\approx 0.02\%$	$\approx 0.02\%$
Asymmetry/fit stability	0.013%	0.013%
Total quadrature	0.065%	0.050%

termined in this fashion to be typically 0.02% for  $nS(6^2P_J)$ , but varies somewhat depending on the total absorption strength which is proportional to density.

Finally, as a measure of the accuracy of the symmetric line shape model and stability of the fitting procedure, the red and blue halves of the transmission spectra are fit independently and examined for systematic deviations. Dividing the absorption lines at the point of maximum absorption, we find an average change in the density-line strength product of  $-0.011\%$  for the red wing, and  $+0.014\%$  for the blue wing relative to the full-spectrum fitted value. No repeatable Lorentzian line shape asymmetries are observed in the residuals of the full-spectrum fits, nor are any significant asymmetries expected at the densities used in this experiment [13,14]. Line profile distortion due to optical pumping effects is similarly not observed at the probe intensities used in these measurements, where a Cs atom typically undergoes four thermalizing wall collisions for each photon scattered. The small differences between the red/blue half fits and the full fit are most likely related to details of the fitting process, such as differences in the shape of  $\chi^2$  surface near the minimum value which depend on truncation of the data set. The error budget includes an additional contribution of 0.013% to account for this variation, which we refer to as ‘‘asymmetry/fit stability.’’ Table I gives a complete summary of the various uncertainty terms described above.

Values of  $nS(6^2P_J)$  obtained from the 69 full-spectrum model fits are tabulated and assigned individual uncertainties as previously outlined. Each group of repeated observations corresponding to a single fine structure component is weighted with the statistical uncertainties of the individual fits and combined in a mean value. The standard error in this weighted mean value is taken as a measure of the stability of the measurement against (real) density fluctuations, and as such contributes an additional uncertainty in determining  $nS(6^2P_J)$  for the ratio measurement. This variance is used to estimate the size of small drifts in the vapor density which may occur during the time required to convert the laser for operation near the other fine structure transitions. The quantities  $nS(6^2P_{1/2})$  and  $nS(6^2P_{3/2})$  measured at seven different stem temperatures (and hence values of the density  $n$ ) form coordinate pairs, with associated uncertainties in each component. A scan with no absorption cell provides an additional point at the origin corresponding to the zero density case, with an uncertainty appropriate to the detection limitations. The plot of  $nS(6^2P_{3/2})$  versus  $nS(6^2P_{1/2})$  is presented in Fig. 7. The slope of this line is the desired ratio  $\mathcal{R}$ , and these pairs are used as input to a linear model which includes the calculated uncertainties in both the abscissa and ordinate.

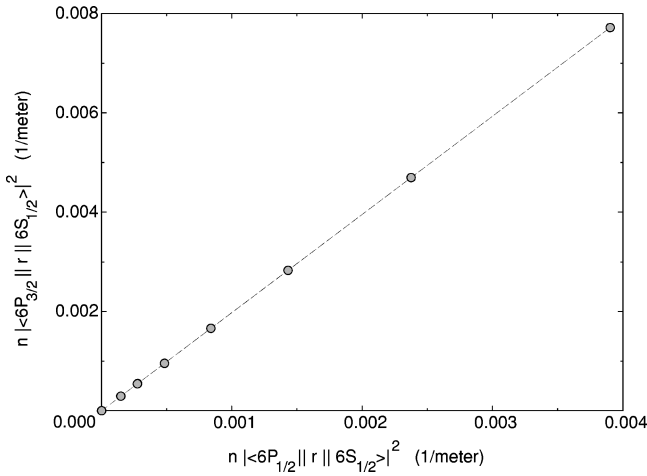


FIG. 7. Ratio line, the plot of  $nS(6^2P_{3/2})$  versus  $nS(6^2P_{1/2})$ . Uncertainties are much smaller than the plotting symbols; the line is the best fit to the data, which has a slope of 1.9809(9) and an intercept consistent with zero.

This procedure is considerably more difficult than linear modeling with measurement uncertainty in only one of the variables, because the partial differential equation for minimization with respect to the slope is in general nonlinear. We use the program FITEXY of Ref. [4], which properly accounts for uncertainty in both the coordinates, and has demonstrated good convergence and confidence-region estimates in fits to simulated data. Figure 8 shows the residuals of this single fit, where, due to the smallness of the error bars in comparison to the magnitude and variation of the quantities  $nS(6^2P_J)$ , two different plots are used to present clearly the deviation in both coordinates. The best fit to the data has a reduced  $\chi^2$  of 1.1, with a slope of  $\mathcal{R}=1.9809(9)$  and an intercept consistent with zero ( $\pm 2 \times 10^{-9}$ ); the quoted uncertainty is the statistical error in fitting the line given the individual uncertainties in the coordinates. The residuals are distributed within reasonable statistical expectations and display no non-linearity or serious systematic dependences with increasing density.

This value of the ratio is found using the various corrections described in the preceding sections—offset drift subtraction, and compensation for finite laser linewidth and magnetic field effects. These corrections have almost no effect on the final ratio value. Using the raw spectra uncorrected for drifting offsets, and fitting with the further assumptions of theoretical Lorentzian widths and perfectly monochromatic laser light, we find a fractional increase in the ratio of only  $6 \times 10^{-4}$ , which is smaller than the combined  $1\sigma$  uncertainty. Correcting the instrumental offset drift only, and retaining the theoretical value of the Lorentzian width and monochromatic laser, we find the ratio is increased by an even smaller fraction of  $4.5 \times 10^{-4}$ , a spread again of less than the statistical uncertainty in the fits. Inclusion of all corrections and best estimates for the magnetic field and laser linewidth recovers the final value.

## V. DISCUSSION AND CONCLUSIONS

Figure 9 displays the present result for the ratio  $\mathcal{R}$  along with other values of the ratio computed from our previous

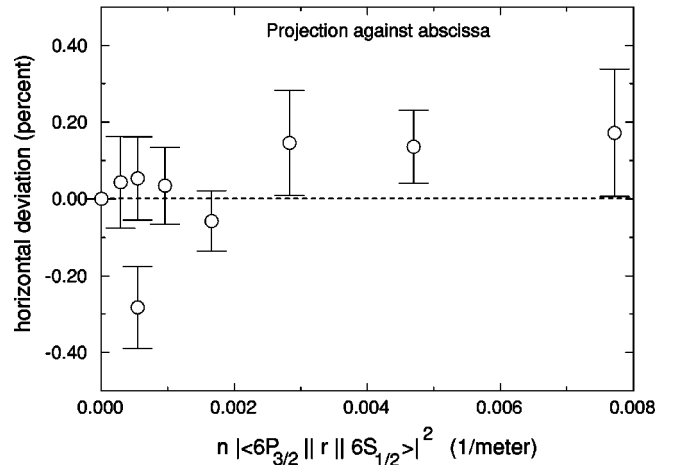
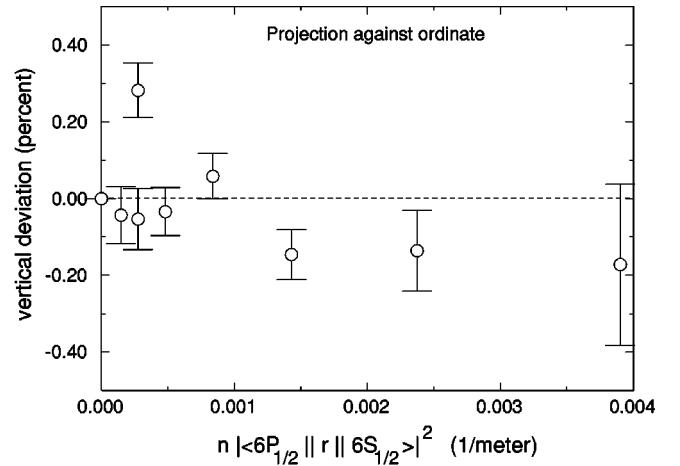


FIG. 8. Residuals of linear fit to plot of  $nS(6^2P_{3/2})$  against  $nS(6^2P_{1/2})$ , with uncertainties in  $x$  and  $y$ .

fast-beam lifetime measurements [6,15], comparable high-precision lifetime measurements [16], an early spectroscopic ratio measurement [17], and atomic theory [18–23]. Our direct-absorption ratio measurement is in excellent agreement with all previous work, and represents a reduction in uncertainty of almost an order of magnitude beyond the best previous measurements.

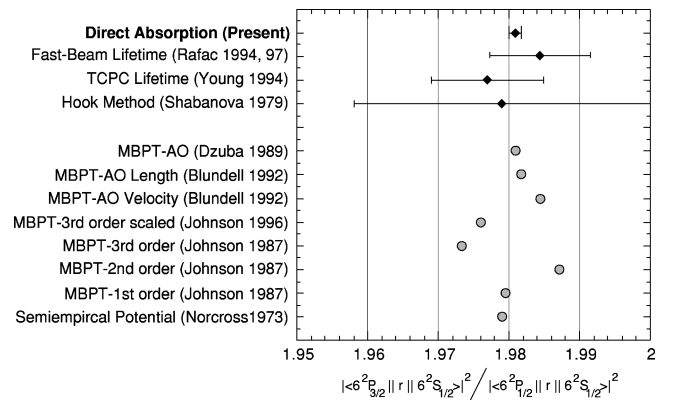


FIG. 9. Comparison of the present measurement of the ratio of  $6^2P$  line strengths with selected experimental and theoretical results.

The current progress of *ab initio* theory in the alkali-metal atoms is plotted in Fig. 10, which shows experimental [16,24–28] and many-body perturbation theory (MBPT) determinations [18,20–22] of the deviation of the  $nP_{3/2}, nP_{1/2}$  ratio from the nonrelativistic expectation of 2:1 for Na, K, Rb, Cs, and Fr. The plotted ratios are also listed in Table II. As anticipated, the ratios in the heavier elements deviate more strongly from the nonrelativistic prediction. There is, in general, good agreement with the calculations, which are thought to be accurate to about 1% in each of the matrix elements. The *ab initio* ratios are therefore determined with a similar precision, but there are reasons to expect that some theoretical systematics may cancel in the ratio, resulting in a somewhat improved value. Assuming for the moment that this is indeed the case, the present results indicate that for the heavy alkali metals, inclusion of third-order diagrams does not improve the agreement with experiment and that calculation of at least some classes of diagrams to all orders is necessary. The correspondence may simply be fortuitous, given estimates of the contributions of diagrams missing from the calculation. The impressive degree of agreement between the two separate all-orders calculations, however, suggest rather strongly that most of the important diagrams are properly accounted for. Inclusion of structural radiation and normalization terms does not significantly affect the ratio in third order, and correction with an empirically scaled Brueckner-orbital contribution improves the situation only marginally [22]. The experimental ratios determined from beam-laser lifetime measurements tend to be somewhat larger than the calculated values for the heavier alkali metals (although not significantly so given the size of the uncertainties); however, the present absorption measurement which is the most accurate falls into the middle of the distribution of theoretical results.

The difference in the ratios obtained by absorption and the average of the best existing lifetime measurements is  $\Delta = 0.0003(53)(9)$ , where the first uncertainty results from the lifetime values [6,15,16] and the second from the absorption measurement. The excellent agreement with independent measurements of the individual transition probabilities indi-

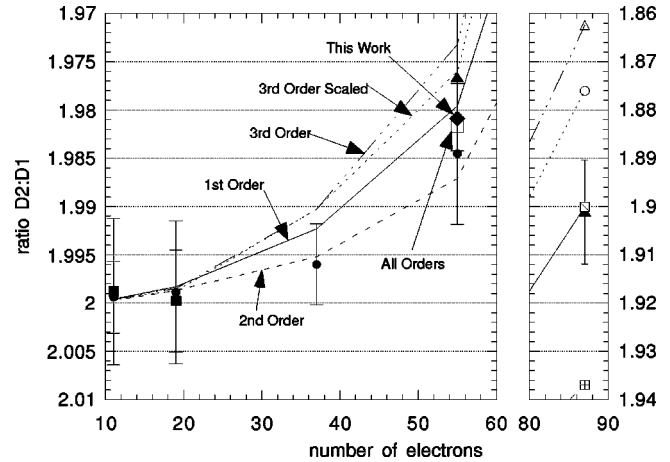


FIG. 10. Progress of MBPT calculations of the ratio of  $D2:D1$  line strengths and comparison with experiment. Error bars are shown only for experimental results. Solid circles with error bars represent the best fast-beam lifetime measurements for Na, K, Rb from [24] and for Cs from [6]. Solid squares are the best determinations from photoassociative spectroscopy, with results for Na from [26,27] and for K from [25]. The solid diamond is the present direct absorption measurement, with an uncertainty smaller than the plotting symbol. First- and second-order theoretical results are taken from [22] for Na, and [21] for all others; all third-order results are from [22]. The cesium all-orders result of [18] is the open square partially obscured by our direct absorption measurement for Cs. Time-resolved lifetime measurements for Cs [16] and Fr [28] are plotted as the solid triangles. For Fr the experimental and theoretical [22] results are plotted to the right with a reduced scale and shifted origin. All theoretical ratios plotted are calculated using the position form of the dipole operator.

cates that the technique is robust enough to be employed as a diagnostic for precise measurements of poorly known line strengths in cesium. Since the  $6^2P_j$  lifetimes are known with a precision of better than 0.25% [6,15,16], other laser-accessible transition strengths can be determined via measurement of the ratio of the desired transition strength to that of either of the well-known  $D$  lines. As can be seen from the

TABLE II. Experimental and theoretical line strength ratios of the  $D2:D1$  transitions in the neutral alkali-metal atoms. All theoretical ratios are calculated using the position form of the dipole operator.

Neutral atom	Experimental ratio $D2:D1$			Order of MBPT				
	Lifetime measurements	Photoassoc. spec.	This work Abs. Spec.	1st	2nd	3rd	3rd+ scaling	All orders
$^{23}_{11}\text{Na}$	1.9994(37) <sup>a</sup>	1.9988(76) <sup>b</sup>		1.9996 <sup>c</sup>	1.9997 <sup>c</sup>	1.9996 <sup>c</sup>	1.9997 <sup>c</sup>	
$^{39}_{19}\text{K}$	1.9989(74) <sup>a</sup>	1.9998(53) <sup>d</sup>		1.9983 <sup>e</sup>	1.9987 <sup>e</sup>	1.9985 <sup>c</sup>	1.9987 <sup>c</sup>	
$^{85}_{37}\text{Rb}$	1.9960(42) <sup>a</sup>			1.9923 <sup>e</sup>	1.9952 <sup>e</sup>	1.9903 <sup>c</sup>	1.9903 <sup>c</sup>	
$^{133}_{55}\text{Cs}$	1.9806(53) <sup>f</sup>		1.9809(9)	1.9796 <sup>e</sup>	1.9871 <sup>e</sup>	1.9732 <sup>c</sup>	1.9760 <sup>c</sup>	1.9817 <sup>g</sup>
$^{210}_{87}\text{Fr}$	1.9011(108) <sup>h</sup>			1.9001 <sup>c</sup>	1.9370 <sup>c</sup>	1.8624 <sup>c</sup>	1.8760 <sup>c</sup>	

<sup>a</sup>Reference [24].

<sup>b</sup>Ratio of Ref. [27] to Ref. [26].

<sup>c</sup>Reference [22].

<sup>d</sup>Reference [25].

<sup>e</sup>Reference [21].

<sup>f</sup>Weighted average of Refs. [6, 16].

<sup>g</sup>Reference [18].

<sup>h</sup>Reference [28].

preceding analysis, the primary error contribution in such a measurement is the uncertainty in the calibrating line strength, provided some important conditions are met. These requirements are related to maintaining the accuracy of the line shape model—the hyperfine structure of the desired excited state must be well known, and the transition must be strong enough (within a few orders of magnitude) in comparison to the calibrating line. Even if these criteria are not perfectly satisfied, a reasonably high precision of  $\approx 1\%$  should still be attainable in many cases. Precision lifetime and hyperfine data are beginning to appear for much weaker optical transitions in Cs (the ground-state excitation to  $5d^2D_J$  is a good example [29]), which may serve as better calibration benchmarks for measurements of very small transition amplitudes, where high vapor densities will necessarily be required. As long as collisional depopulation effects remain in the linear (impact) regime the line shape model

described here should remain accurate, and these mechanisms are in any event accessible to measurement in the same apparatus. We expect this technique to be instrumental in obtaining high-quality results in measurements of the  $6^2S_{1/2}$ - $7^2P_J$  transition strength, and of the  $6^2S_{1/2}$ - $7^2S_{1/2}$  Stark polarizabilities, experiments which are currently underway in our laboratory.

#### ACKNOWLEDGMENTS

We thank W. R. Johnson, J. Sapirstein, A. E. Livingston, and H. G. Berry for helpful discussions. We also thank J. Simsarian for communicating his results to us prior to publication. R.J.R. thanks the Arthur J. Schmitt Foundation for financial support. This research was made possible by the National Science Foundation under Contract No. PHY95-04889.

- 
- [1] C. S. Wood, Ph.D. thesis, University of Colorado, 1996.  
 [2] C. S. Wood *et al.*, *Science* **275**, 1759 (1997).  
 [3] P. Meystre and M. Sargent III, in *Elements of Quantum Optics*, 1st ed. (Springer-Verlag, New York, 1990), p. 7.  
 [4] W. H. Press, S. A. Teukolsky, W. T. Vetterling, and B. P. Flannery, *Numerical Recipes in FORTRAN*, 2nd ed. (Cambridge University Press, New York, 1992).  
 [5] C. Chiarella and A. Reichel, *Math. Comput.* **22**, 137 (1968).  
 [6] R. J. Rafac, Ph.D. thesis, University of Notre Dame, 1997.  
 [7] W. A. van Wijngaarden, *Bull. Am. Phys. Soc.* **40**, 1272 (1995).  
 [8] W. A. van Wijngaarden and J. Li, *J. Opt. Soc. Am. B* **11**, 2163 (1994).  
 [9] R. J. Rafac and C. E. Tanner, *Phys. Rev. A* **56**, 1027 (1997).  
 [10] C. E. Tanner and C. Wieman, *Phys. Rev. A* **38**, 1616 (1988).  
 [11] C. G. Carrington, D. N. Stacey, and J. Cooper, *J. Phys. B* **6**, 417 (1973).  
 [12] C. Leahy, J. T. Hastings, and P. M. Wilt, *Am. J. Phys.* **65**, 367 (1997).  
 [13] K. Niemax and G. Pilcher, *J. Phys. B* **7**, 1204 (1974).  
 [14] K. Niemax and G. Pilcher, *J. Phys. B* **7**, 2355 (1974).  
 [15] R. J. Rafac *et al.*, *Phys. Rev. A* **50**, R1976 (1994).  
 [16] L. Young *et al.*, *Phys. Rev. A* **50**, 2174 (1994).  
 [17] L. N. Shabanova, Y. N. Monakov, and A. N. Khlyustalov, *Opt. Spectrosc.* **47**, 1 (1979).  
 [18] S. A. Blundell, J. Sapirstein, and W. R. Johnson, *Phys. Rev. D* **45**, 1602 (1992).  
 [19] S. A. Blundell, W. R. Johnson, and J. Sapirstein, *Phys. Rev. A* **43**, 3407 (1991).  
 [20] V. A. Dzuba, V. V. Flambaum, A. Y. Kraftmakher, and O. P. Shushkov, *Phys. Lett. A* **147**, 373 (1989).  
 [21] W. R. Johnson, M. Idrees, and J. Sapirstein, *Phys. Rev. A* **35**, 3218 (1987).  
 [22] W. R. Johnson, Z. W. Liu, and J. Sapirstein, *At. Data Nucl. Data Tables* **64**, 279 (1996).  
 [23] D. W. Norcross, *Phys. Rev. A* **7**, 606 (1973).  
 [24] U. Volz and H. Schmoranzler, *Phys. Scr.* **T65**, 48 (1996).  
 [25] H. Wang *et al.*, *Phys. Rev. A* **55**, R1569 (1997).  
 [26] E. Tiemann, H. Knoeckel, and H. Richling, *Z. Phys. D* **37**, 323 (1996).  
 [27] K. M. Jones *et al.*, *Europhys. Lett.* **35**, 85 (1996).  
 [28] J. E. Simsarian *et al.*, *Phys. Rev. A* **57**, 2448 (1998).  
 [29] D. DiBerardino, C. E. Tanner, and A. Sieradzan, *Phys. Rev. A* **57**, 4204 (1998).